Supplementary information for: Topological Isomerization Unlocks Exceptional Elasticity and Strength of Cellulosic Triboelectric Aerogels

Qiguan Luo[1], Feng Gao[1], Zheying Liu[1], Tao Liu[1], Song Zhang[1], Bin Luo[1], Chenchen Cai[1], Jinlong Wang[1],Yanhua Liu[1], Yayu Bai[1], Kang Yu[1], and Shuangxi Nie[1]*

[1]Guangxi Key Laboratory of Clean Pulp & Papermaking and Pollution Control, School of Light Industry and Food Engineering, Guangxi University, Nanning, 530004 China

E-mail: nieshuangxi@gxu.edu.cn

SUPPLEMENTARY INFORMATION

This file includes:

Supplementary Note 1: Calculation of crystallinity

Supplementary Note 2: Molecular dynamics simulation details

Supplementary Note 3: Finite element simulation details

Supplementary Note 4: Density functional theory calculations details

Supplementary Note 5: Calculation of hydrogen bond Energy and bond length

Supplementary Figure 1 to 32

Supplementary Table 1 to 7

Other Supplementary Materials for this manuscript include:

Supplementary Movie 1 to 5

Supplementary Note 1: Calculation of crystallinity

To determine the crystallinity (*Cr*) of cellulose, the DMFIT program was used to unfold the spectrum. The peak areas ranging from 82.7 to 76.2 ppm correspond to the proportion of the amorphous region of C4 atoms in the sample ($X_{\text{amorphous}}$). The calculation formula for *Cr* is as follows[1]:

$$Cr = 100\% - X_{\text{amorphous}} \quad (1)$$

The crystallinity (*Cr*) of CNF-I and CNF-III is 73.1% and 45.8%, respectively.

Supplementary Note 2: Molecular dynamics simulation details

Molecular dynamics simulations were conducted on CNF-I and CNF-III to characterize structural and dynamical features of both allomorphs. The models comprised 30 (6 × 5) octameric glucan chains for each cellulose polymorph, with crystallographic parameters obtained from literatures and subsequently optimized[2,3]. The refined parameters are documented in Supplementary Table 6 and 7. All simulations utilized the CVFF force field within the LAMMPS software package under NPT conditions. Temperature and pressure were regulated by a Langevin thermostat (damping coefficient = 1.0 ps^{-1}) and a Nosé-Hoover-Langevin barostat with stochastic components (oscillation period = 200 fs, damping period = 100 fs), respectively. Nonbonded interactions employed a 10.0 Å cutoff in coordinate space, with periodic boundary conditions applied throughout.

The fibrils were solvated in a rectangular water box, and each octameric cellulose chain was covalently connected to its periodic image along its main axis in order to mimic an infinitely long cellulose fibril. The solvated cellulose fibrils underwent first a local

optimization, followed by a short (~0.5 ns) NPT-MD simulation, where the temperature was gradually increased from 100 to 298 K, and by a 200 ns long NPT-MD simulation at T = 298 K and P = 1.01325 bar. The first 20 ns of the 200 ns run was considered the equilibration period, with the remaining 180 ns used for production. The timestep was fixed at 2.0 fs. The covalent bonds involving hydrogen atoms were constrained by means of the SHAKE algorithm.

The torsion angles χ: O5–C5–O6–C6 and χ′: C4–C5–O6–C6 govern the conformation of the C6 primary hydroxyl group. Standard *tg* and *gt* conformations are defined by angle sets (180°, -60°) and (60°, 180°), respectively. The glycosidic torsion angles φ: O5–C1–O1–C4 and ψ: C1–O1–C4–C3 describe the linkage conformation between adjacent glucose monomers within a chain, characterizing the relative orientation of glucosyl residues[4]. Simulations revealed distinct hydroxymethyl conformations (Table S3 and S4): CNF-I: χ = 165.6°, χ′ = -70.61°, dominant *tg* conformation. CNF-III: χ = 53.5°, χ′ = 169.26°, with a dominant *gt* conformation.

Supplementary Note 3: Finite element simulation details

To illustrate the stress distribution during the compression of honeycomb aerogels and to analyze their structural stability, finite element simulations of this physical process were performed using COMSOL Multiphysics software. A porous 3D cubic model with a side length of 2 cm (Supplementary Fig. 32) was established to demonstrate the deformation process of the aerogel and its unique pore structure under solid mechanics physical fields. A honeycomb-structured porous aerogel 3D model (Supplementary Fig. 32) was created, and its pore configuration was modified for a comparative

demonstration of structural deformation and physical field distribution during compression.

Supplementary Note 4: Density functional theory calculations details

Cellulose is a macromolecular polymer that is linked to a glucose monomer as a basic unit that incorporates a β-O-4 glycosidic bond. To balance computational efficiency and cost, and in line with previous studies[5–7], cellobiose was selected as the computational model for the analysis of cellulose I and cellulose III. Cellobiose represents the fundamental repeating unit of cellulose and fully incorporates the characteristic β-O-4 glycosidic linkages as well as all key chemical functional groups along the cellulose molecular chains. Although this simplified model cannot fully capture the long-chain conformations of cellulose nanofibrils (CNF-I and CNF-III), its electronic structure analysis provides important molecular-level insights into the intrinsic reactivity of cellulose.

For the CNF-III@Si system, we constructed three representative models to facilitate a comprehensive analysis that aligns more closely with the material's potential structures, rather than relying on a single model. The first model features an ungrafted CNF-III chain, represented by a single fiber tetrasaccharide unit. In the second model, a -$Si(OH)_2CH_3$ group is grafted onto the fiber tetrasaccharide skeleton, denoted as CNF-III@Si-1. The third model, referred to as CNF-III@Si-2, involves siloxane grafting at all C6 sites of the tetrasaccharide unit to simulate a cross-linked polymer network structure. The simplification of these models reflects a balance between computational resource limitations and the necessity for atomic-level analysis of core interactions.

Additionally, for regular polymers such as fluorinated ethylene propylene (FEP), this study employs their periodic repeating units as the computational model, a widely accepted approach in DFT calculations for examining the electronic structure of polymers.

All of the density functional theory (DFT) calculations were carried out with Materials Studio DMol^3 program from Accelrys[8,9]. All initial structures were fully geometry-optimized prior to electronic structure analysis to obtain energetically stable conformations. Geometry optimizations were performed using the hybrid exchange–correlation functional B3LYP in combination with a double numerical basis set with polarization functions (DNP). The geometry optimizations were considered converged when the total energy, maximum force, and maximum displacement reached 1.0×10^{-5} Ha, 0.002 Ha Å^{-1}, and 0.005 Å, respectively. The self-consistent field convergence threshold was set to 1.0×10^{-5} Ha.

The conformational activity was evaluated using the energy gap (E_{gap}, eV)[10]:

$$E_{gap} = E_{LUMO} - E_{HOMO} \tag{2}$$

where E_{HOMO} and E_{LUMO} are the energies (eV) of the highest occupied molecular orbital (HOMO) and the lowest unoccupied molecular orbital (LUMO), respectively. E_{gap} is an important stability index in chemical reactions, and a larger E_{gap} indicates enhanced molecular stability and reduced chemical reactivity. The electron gain/loss capacity of the derivatives was evaluated using HOMO and Fukui function. A larger HOMO value and the more Fukui function distribution indicate a greater likelihood of losing electrons.

The electrostatic potential (ESP) distributions of the optimized CNF-III derivative models were calculated based on the converged electron density. The ESP was mapped onto the molecular electron density is surface to visualize the spatial variation of electrostatic potential over the molecular surface. All ESP calculations were performed on the optimized neutral structures without further structural relaxation.

The Fukui functions were calculated to evaluate the local chemical reactivity of different atomic sites in the CNF-III derivative models. A finite difference approach was employed by performing additional single-point calculations for the anion (N + 1 electrons) and cation (N − 1 electrons) states based on the optimized neutral geometries. The Fukui functions corresponding to nucleophilic $(f^+)$and electrophilic (f^-)attacks were defined as:

$$f^+ = \rho(N+1) - \rho(N) \quad (3)$$

$$f^- = \rho(N) - \rho(N-1) \quad (4)$$

where $\rho(N)$, $\rho(N+1)$, and $\rho(N-1)$denote the electron densities of the neutral, anionic, and cationic states, respectively. All charged-state calculations were carried out without further geometry optimization to ensure consistent comparison of electron density distributions.

Supplementary Note 5: Calculation of hydrogen bond energy and bond length

To better understand the changes in the hydrogen bonds, deconvolution of the spectra (3800–3000 cm^{-1}) was performed using PeakFit software with a Gaussian distribution function to analyze hydrogen bond strength, bond energies (E_H) and bond lengths (R)

for different hydrogen bond models. After deconvolution, hydrogen bond characteristic parameters were calculated as follows[11]:

$$E_{\mathrm{H}} = \frac{v_0 - v}{kv_0} \tag{5}$$

where v_0 is standard free hydroxyl (–OH) frequency (3650 cm^{-1}), v is the sample hydroxyl (–OH) frequency, and k is constant (3.82×10^3 kJ^{-1}).

$$\Delta v\ (cm^{-1}) = 4.43 \times 10^3 (2.83 - R) \tag{6}$$

where $\Delta v = v_0 - v$, v_0 is stretch vibrational frequencies of hydroxyl at 3600 cm^{-1}, and v is the sample hydroxyl (–OH) frequency[11].

During treatment with ethylenediamine, the crystal structure of cellulose I underwent a rearrangement, transforming into cellulose III, characterized by significant reconstruction of its hydrogen bond network. The strength of typical hydrogen bonds in cellulose varies, with O(2)H···O(6) being the weakest, followed by O(3)H···O(5), and O(6)H···O(3′) as the strongest. Statistical analyses indicate that following the crystal transformation, the proportion of O(2)H···O(6) hydrogen bonds increased significantly from 7.5% to 10.6%. In contrast, the proportions of O(3)H···O(5) and O(6)H···O(3′) hydrogen bonds decreased by approximately 2% and 1%, respectively. This alteration primarily results from the perturbative effect of ethylenediamine molecular intercalation on the original hydrogen bond network.

Upon the incorporation of ethylenediamine into the cellulose molecular chains, the interchain spacing increases, thereby weakening the highly ordered and geometrically constrained interchain hydrogen bonds O(6)H···O(3′) present in cellulose I. Concurrently, this incorporation induces a degree of conformational relaxation, which

reduces the stability of the moderately strong intrachain hydrogen bonds O(3)H···O(5). This observation aligns with the trends in the distribution of intramolecular hydrogen bonds and the quantity of interlayer hydrogen bonds observed in the molecular dynamics (MD) simulation results. In contrast, the O(2)H···O(6) hydrogen bonds exhibit lower requirements for intermolecular spacing and orientation, making them more readily formed under conditions of crystal structure relaxation and increased molecular chain mobility. The increased proportion of these bonds partially compensates for the structural stability loss resulting from the reduction of strong hydrogen bonds. This alteration is consistent with the observed changes in the number of intramolecular hydrogen bonds and the transformation of conformational freedom in the MD simulation. Collectively, these findings indicate that the transition from cellulose I to cellulose III is characterized by a shift from a robust and ordered hydrogen bond network to a more abundant and lower-energy weak hydrogen bond network, which represents a significant aspect of the crystal structure characteristics of cellulose III.

Supplementary Figure 1 to 32

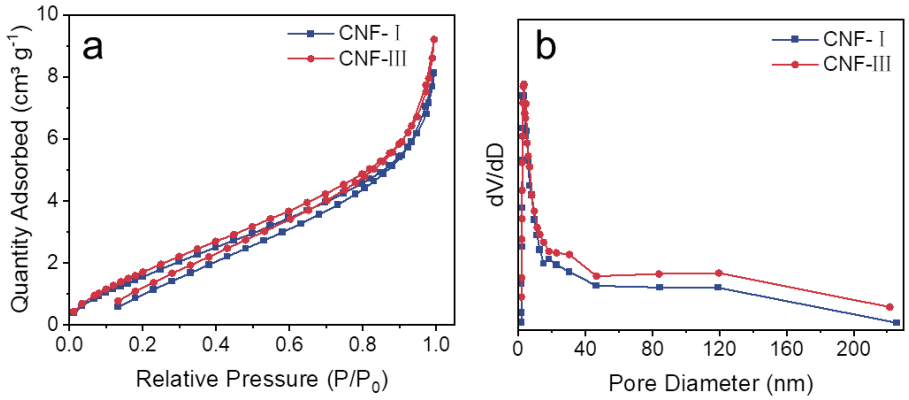

Supplementary Figure 1. Nitrogen adsorption-desorption curves (**a**) and pore diameter distribution (**b**) of CNF-I and CNF-III aerogels. The BET specific surface areas of CNF-I and CNF-III aerogels are 6.8 ± 0.1 m^2 g^{-1} and 7.5 ± 0.1 m^2 g^{-1}, respectively. Due to the destruction of the hydrogen bond network by amine treatment, the specific surface area of CNF-III is about 10% higher than that of CNF-I, but the curve shape and coincidence indicate that the microstructure has hardly changed significantly. The cumulative volume of void adsorption calculated by the BJH method is 0.015 cm^3 g^{-1} and 0.017 cm^3 g^{-1}, respectively (pore size range 1.7 ~ 300.0 nm), which indicates that the EDA treatment has not caused a significant change in the pore structure.

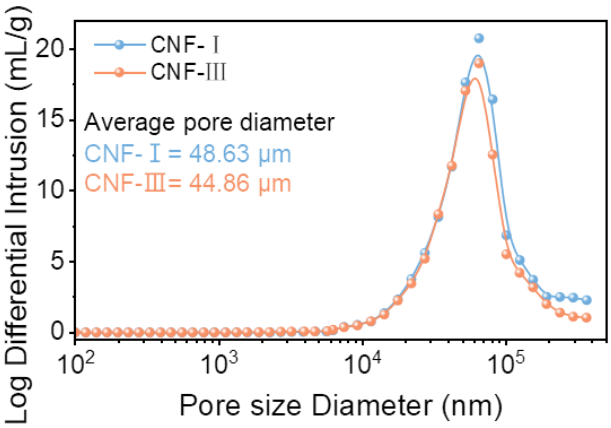

Supplementary Figure 2. Pore size distribution of CNF-I and CNF-III aerogels.

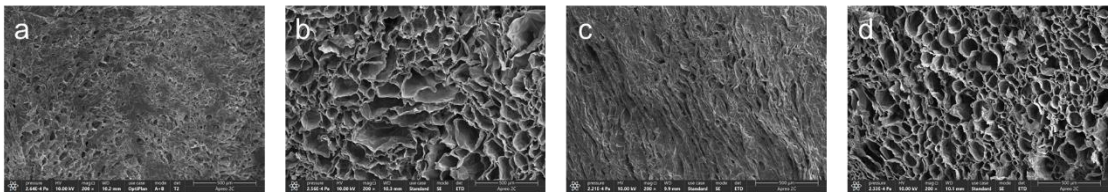

Supplementary Figure 3. SEM images of aerogels before and after ethylenediamine treatment. (**a**, **b**) CNF-I aerogel outer wall (**a**) and axial pore structure (**b**). (**c**, **d**) CNF-III aerogel outer wall (**c**) and axial pore structure (**d**). There was no significant change in the outer wall fiber structure, fiber aggregation state, pore structure, and pore size of CNF-I aerogel and CNF-III aerogel, indicating that the microstructure of the aerogel was not destroyed before and after ethylenediamine treatment.

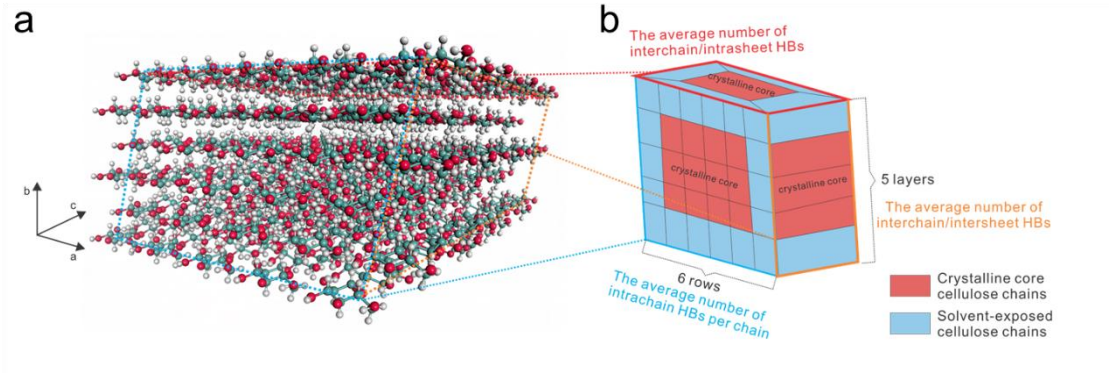

Supplementary Figure 4. (**a**) A molecular dynamics model exemplified by CNF-I. (**b**) A schematic representation illustrating the distribution of molecular chains and hydrogen bonds within cellulose crystals. Molecular chain distribution: the structure comprises five layers, each containing six octamer cellulose chains. The central chains, depicted in red, serve as the core chains, while the outer chains, shown in blue, are exposed to the solvent. Hydrogen bond distribution: the left 6×5 grid (representing the ab-plane of the crystal) indicates the average number of intra-chain hydrogen bonds per chain; the right five layers (representing the bc-plane of the crystal) illustrate the average number of hydrogen bonds between adjacent chains within each layer; the upper section displays the average number of hydrogen bonds between adjacent chains within the same layer (the ac-plane of the crystal).

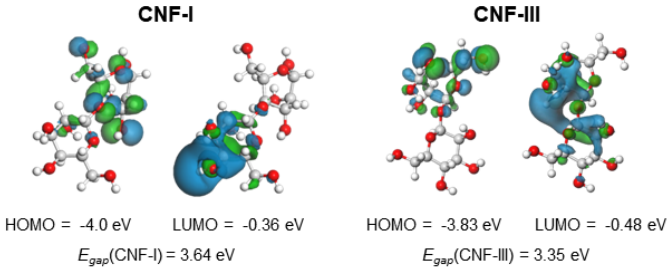

Supplementary Figure 5. The highest occupied molecular orbital (HOMO) and the lowest unoccupied molecular orbital (LUMO) of CNF-I and CNF-III were analyzed to determine the energy band gap (E_{gap}), calculated as $E_{gap} = E_{LUMO} - E_{HOMO}$, where E_{LUMO} represents the energy of the LUMO and E_{HOMO} denotes the energy of the HOMO.

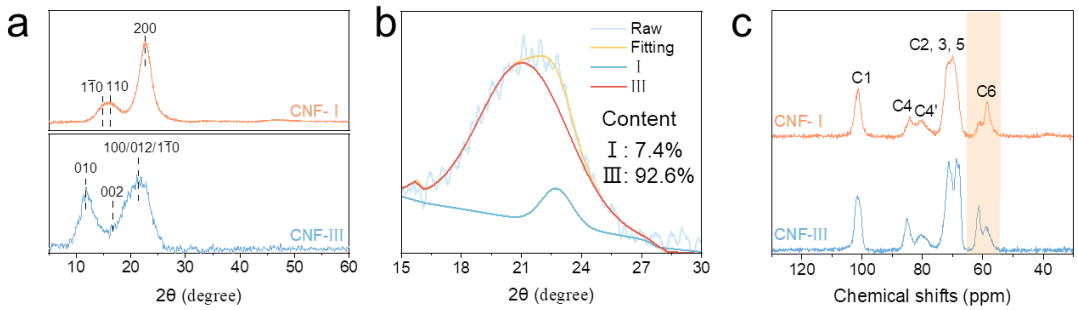

Supplementary Figure 6. (**a**) The XRD patterns of CNF-I and CNF-III. (**b**) The peak fitting of the XRD spectrum of CNF-III aerogel in the range of 15–30°. (**c**) Solid ^{13}C CP/MAS NMR spectra of CNF-I and CNF-III. The crystal conversion rate is the proportion of cellulose III in the CNF-III sample, which is based on the ratio of the peak area of 2θ = 21.0° to the sum of the peak areas of 2θ = 21.0° and 2θ = 22.5° in the XRD spectrum of CNF-III. Cellulose I and cellulose III account for 7.4% and 92.6% respectively, which indicates that most of cellulose I is converted into cellulose III.

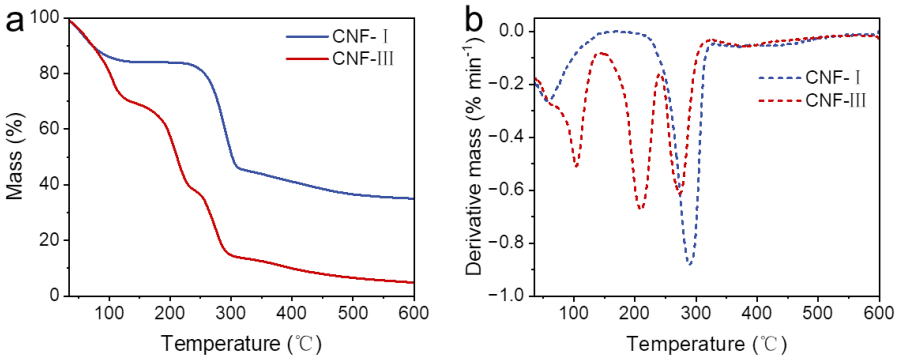

Supplementary Figure 7. TG (**a**) and DTG (**b**) curves of CNF-I and CNF-III aerogels.

The pyrolysis temperature of CNF-I is about 288 ℃, while the pyrolysis temperature of CNF-III drops to 210 ℃, indicating that the flexibility of CNF-III molecules is significantly higher than that of CNF-I. The TGA results indicate that the thermal degradation process of CNF-III can be categorized into four distinct stages. The first stage, occurring at temperatures below 100 °C, corresponds to the removal of adsorbed and bound water within the material. The second stage pertains to the thermal behavior of residual components in the aerogel, where residual amines may exert an autocatalytic degradation effect on the amorphous regions of cellulose. The third stage is associated with the decomposition of cellulose crystalline components. The final stage encompasses the carbonization process of the material. In comparison to CNF-I, CNC-III exhibits a lower pyrolysis char residue following thermal degradation, likely due to its looser crystal structure, which renders it more vulnerable to damage and degradation at elevated temperatures.

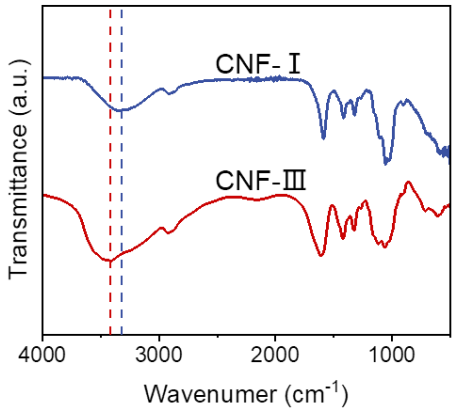

Supplementary Figure 8. FTIR spectra of CNF-I and CNF-III.

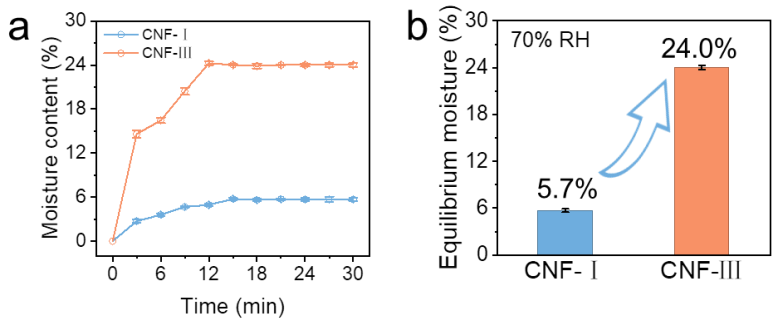

Supplementary Figure 9. Static moisture absorption test of CNF-I and CNF-III aerogels in saturated salt solution at 25 ℃ and 70% relative humidity. (**a**) Change in water content over time. (**b**) Equilibrium water content (distinct samples, mean ± s.d., n = 3 independent experiments).

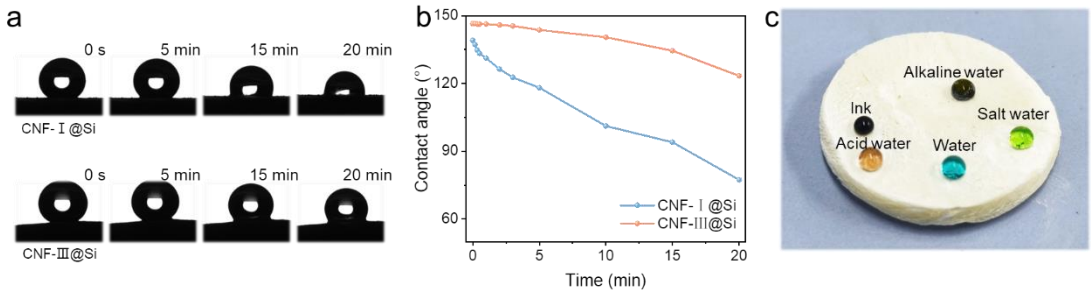

Supplementary Figure 10. Photographs (**a**) and change curves (**b**) of water contact angles on the surfaces of CNF-I@Si and CNF-III@Si aerogels from 0 to 20 min; (**c**) Photographs of different liquids (water (cyan), ink (black), acid solution (yellow), alkaline solution (dark green), and salt solution (green)) dropped onto the surface of CNF-III@Si aerogels. The water contact angle of CNF-I@Si aerogels changed significantly within 20 min (from 139° to 77°), while the contact angle of CNF-III@Si aerogels only decreased from 149° to 123°. Water contact angle experiments show that low hydroxyl accessibility makes it difficult to construct a stable hydrophobic $Si(CH_3)$–O–$Si(CH_3)$ cross-linked network on the surface of CNF-I. The high hydroxyl accessibility of CNF-III can hydrolyze and chemically cross-link MTMS on its surface to form a stable and dense hydrophobic $Si(CH_3)$–O–$Si(CH_3)$ network.

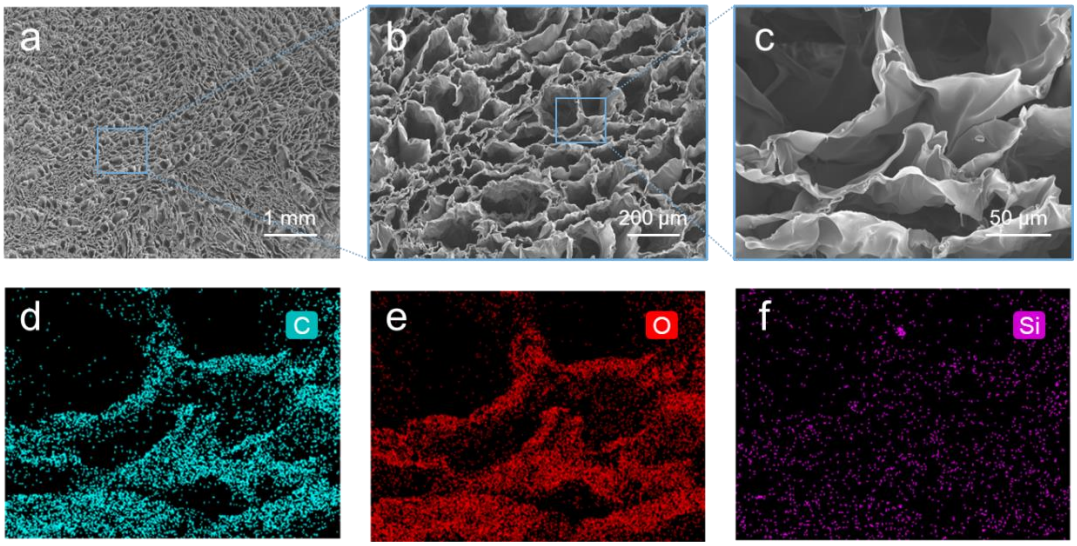

Supplementary Figure 11. (**a-c**) SEM images of CNF-I@Si aerogel. (**b**) and (**c**) are magnified local images of (**a**) and (**b**), respectively. (**d-f**) EDS elemental distribution based on (**c**): (**d**) C, (**e**) O, (**f**) Si.

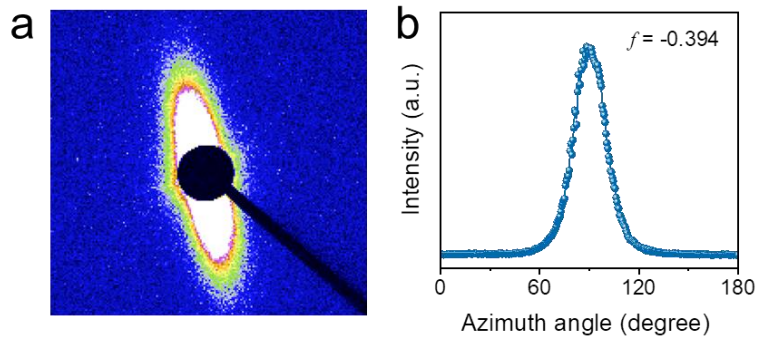

Supplementary Figure 12. 2D SAXS pattern (**a**) and Azimuthal plot (**b**) of CNF-III@Si aerogel. The formula for calculating the Hermann orientation factor (f) is as follows[12]:

$$f = \frac{3(cos^2\varphi)-1}{2} \tag{7}$$

where $(\cos^2\varphi)$ denotes the average of the squares of the cosine function of the azimuth angle from 0 to π/2, and its calculation formula is:

$$(cos^2\varphi) = \frac{\int_0^{\frac{\pi}{2}} I(\varphi)cos^2\varphi \sin\varphi d\varphi}{\int_0^{\frac{\pi}{2}} I(\varphi)sin\,\varphi d\varphi} \tag{8}$$

where $I(\varphi)$ is the intensity at azimuth angle φ. The computed value of f is -0.394, suggesting that the aerogel demonstrates a distinct structural orientation following directional freezing.

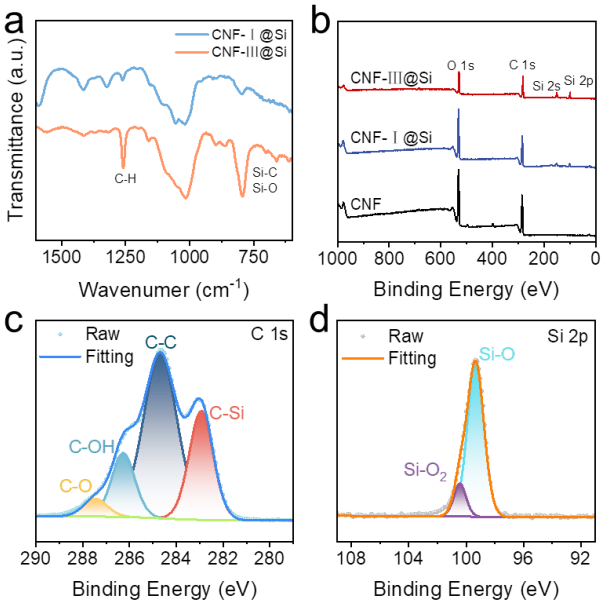

Supplementary Figure 13. (**a**) The FTIR spectra of CNF-I@Si and CNF-III@Si. (**b**) The XPS spectra of CNF-I, CNF-I@Si and CNF-III@Si aerogels. C1s (**c**) and Si2p (**d**) spectrum in the XPS spectrum of CNF-I@Si aerogel, respectively.

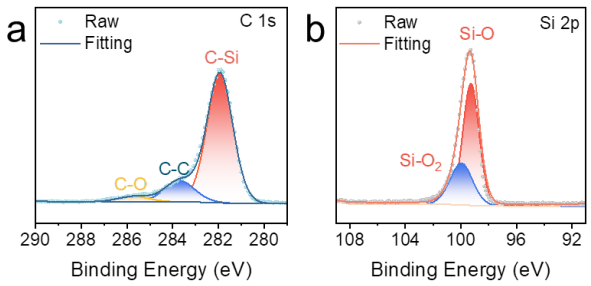

Supplementary Figure 14. C1s (**a**) and Si2p (**b**) spectrum in the XPS spectrum of CNF-III@Si aerogel.

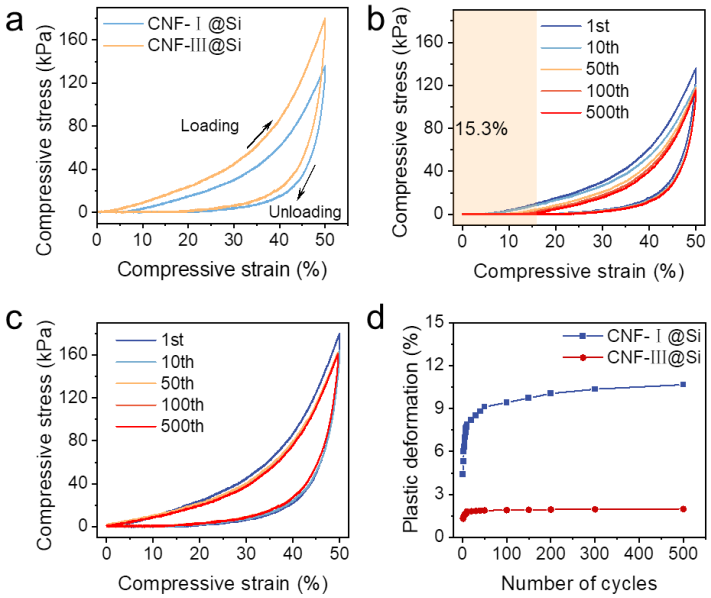

Supplementary Figure 15. (**a**) Stress-strain curves of CNF-I@Si and CNF-III@Si aerogels. Stress-strain curves of CNF-I@Si (**b**) and CNF-III@Si aerogels (**c**) for the first 500 cycles of compression. (**d**) Plastic deformation of CNF-I@Si and CNF-III@Si aerogels for the 500 cycles of compression.

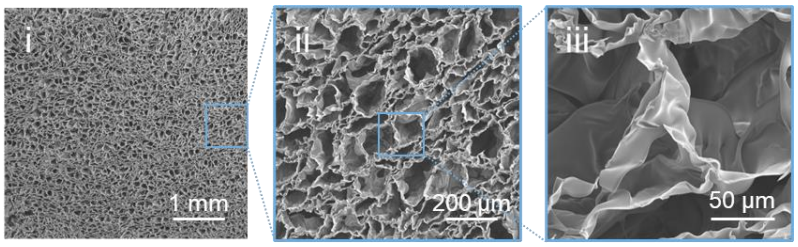

Supplementary Figure 16. SEM images of CNF-III@Si aerogel before cyclic compression.

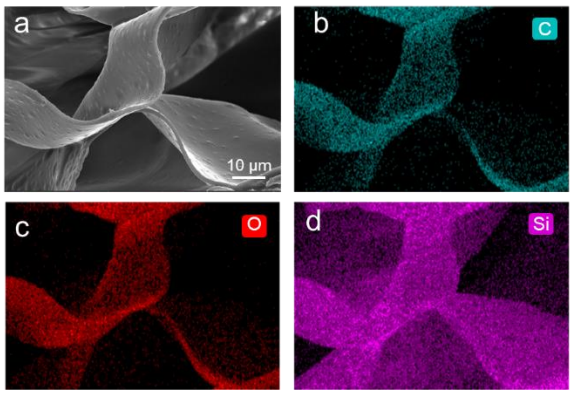

Supplementary Figure 17. (**a**) SEM images of the pore microstructure of CNF-III@Si aerogel after 20,000 compressions. EDX mappings of (**b**) O, (**c**) C, and (**d**) Si.

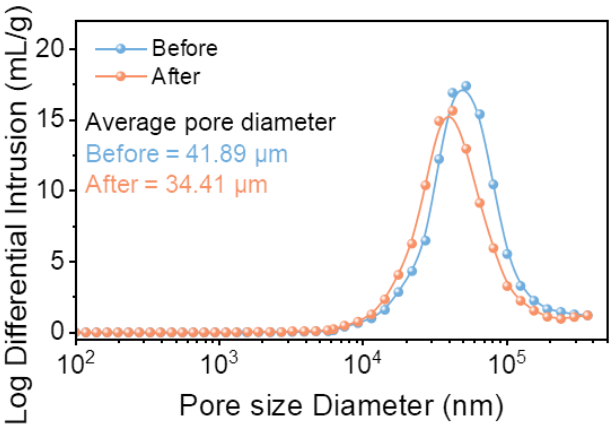

Supplementary Figure 18. Pore diameter distribution of CNF-III@Si before and after cyclic compression.

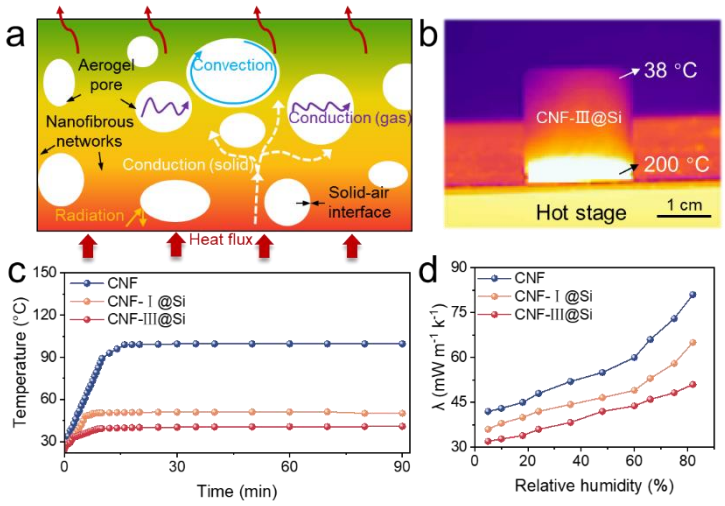

Supplementary Figure 19. **The thermal insulation performance of aerogel.** (**a**) Thermal insulation mechanism. Thermal conductivity is primarily composed of solid-phase conduction (λ_s), gas-phase conduction (λ_g), thermal convection (λ_c), and thermal radiation (λ_r). (**b**) The infrared thermal imaging image of CNF-III@Si aerogel on a hotplate. (**c**) The top temperature of CNF, CNF-I@Si and CNF-III@Si aerogels changes over time. (**d**) Thermal conductivity at different relative humidities. Test results indicate that the axial and radial thermal conductivities are 0.0320 and 0.0328 $W \cdot m^{-1} \cdot K^{-1}$, respectively. These low values suggest that the material exhibits excellent thermal insulation performance in both directions. From a microstructural perspective, the axial direction provides a defined heat transfer path due to the presence of directional pore channels. However, the high porosity and discontinuous solid skeleton lead to significant interfacial thermal resistance, which impedes efficient heat conduction. In contrast, although radial heat flow interacts more frequently with the pore walls and fiber connections, the low solid content and extensive gas-solid interface also restrict phonon transmission. Consequently, bidirectional heat transfer is predominantly governed by gas phase conduction and interfacial scattering, rather than the

discontinuous solid path, resulting in similar axial and radial thermal conductivities. This nearly isotropic low thermal conductivity characteristic offers advantages in practical applications, as it reduces sensitivity to installation direction while ensuring uniform thermal insulation performance.

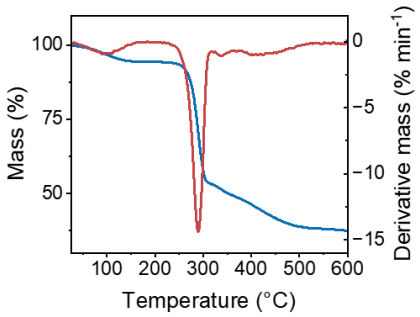

Supplementary Figure 20. TG and DTG curves of CNF-III@Si aerogel.

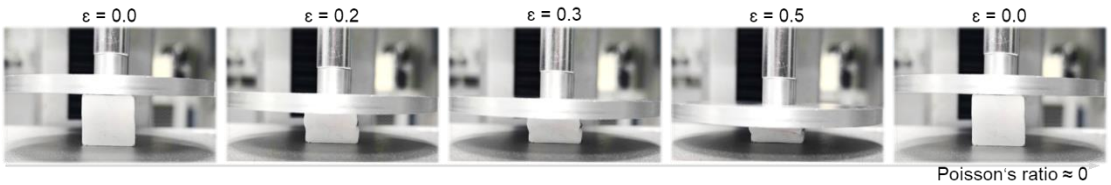

Supplementary Figure 21. Digital photos of the CNF-III@Si aerogel cyclic compression process.

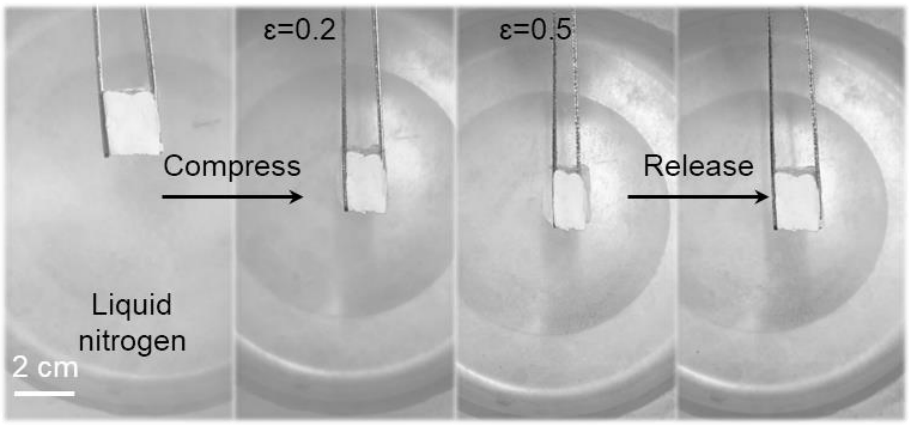

Supplementary Figure 22. The CNF-III@Si aerogel was squeezed in liquid nitrogen (-196 ℃) and returned to its original shape after release.

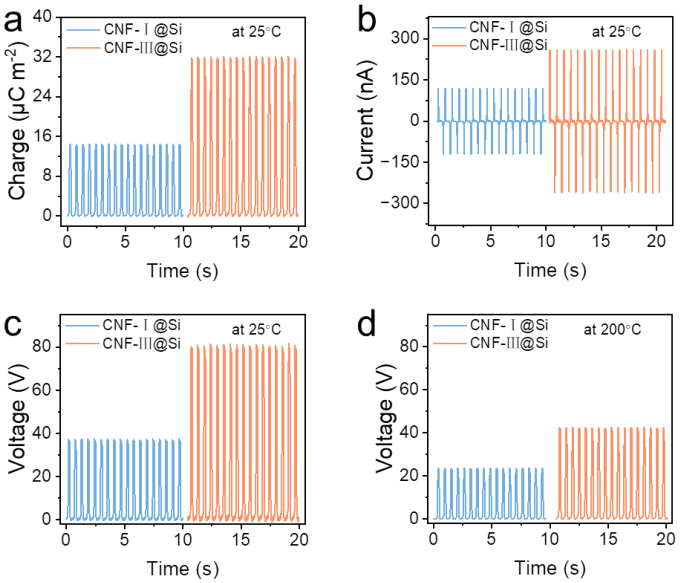

Supplementary Figure 23. Surface charge density (**a**), output current (**b**), and output voltage (**c**) of TENGs based on CNF-I@Si and CNF-III@Si aerogels at 25 °C. (**d**) Output voltage of TENGs based on CNF-I@Si and CNF-III@Si aerogels at 200 °C.

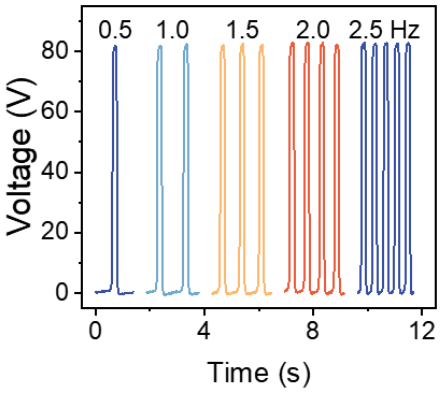

Supplementary Figure 24. Output voltage of TENG at different frequencies based on CNF-III@Si aerogel.

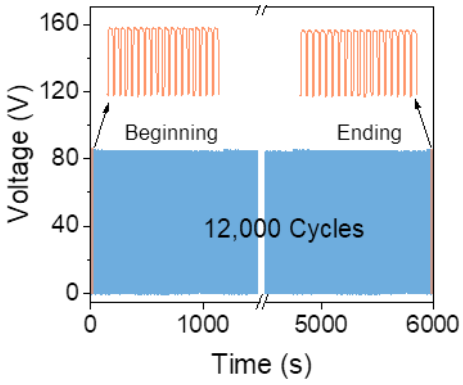

Supplementary Figure 25. The output voltage of the 12,000-cycle test.

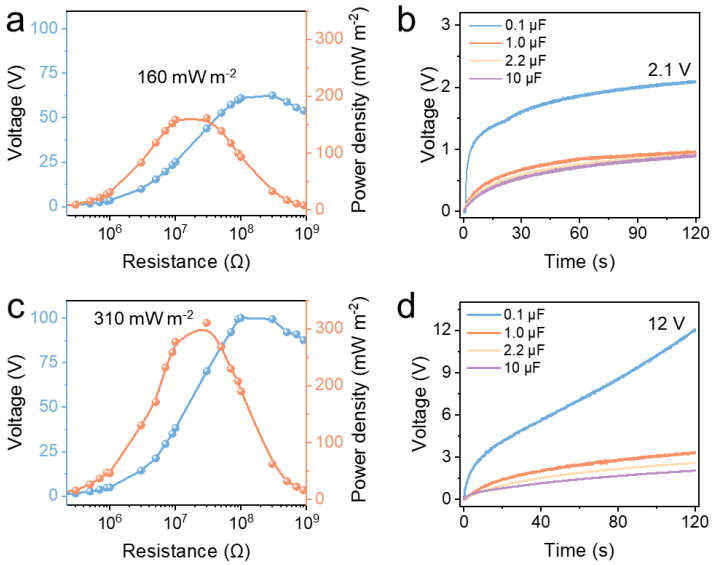

Supplementary Figure 26. (**a**) Output voltage and power density of the CNF-III@Si aerogel-based TENG under different external resistances. (**b**) Capacitor charging curve of the CNF-I@Si aerogel-based TENG. (**c**) Output voltage and power density of the CNF-III@Si aerogel-based TENG under different external resistances. (**d**) Capacitor charging curve of the CNF-III@Si aerogel-based TENG.

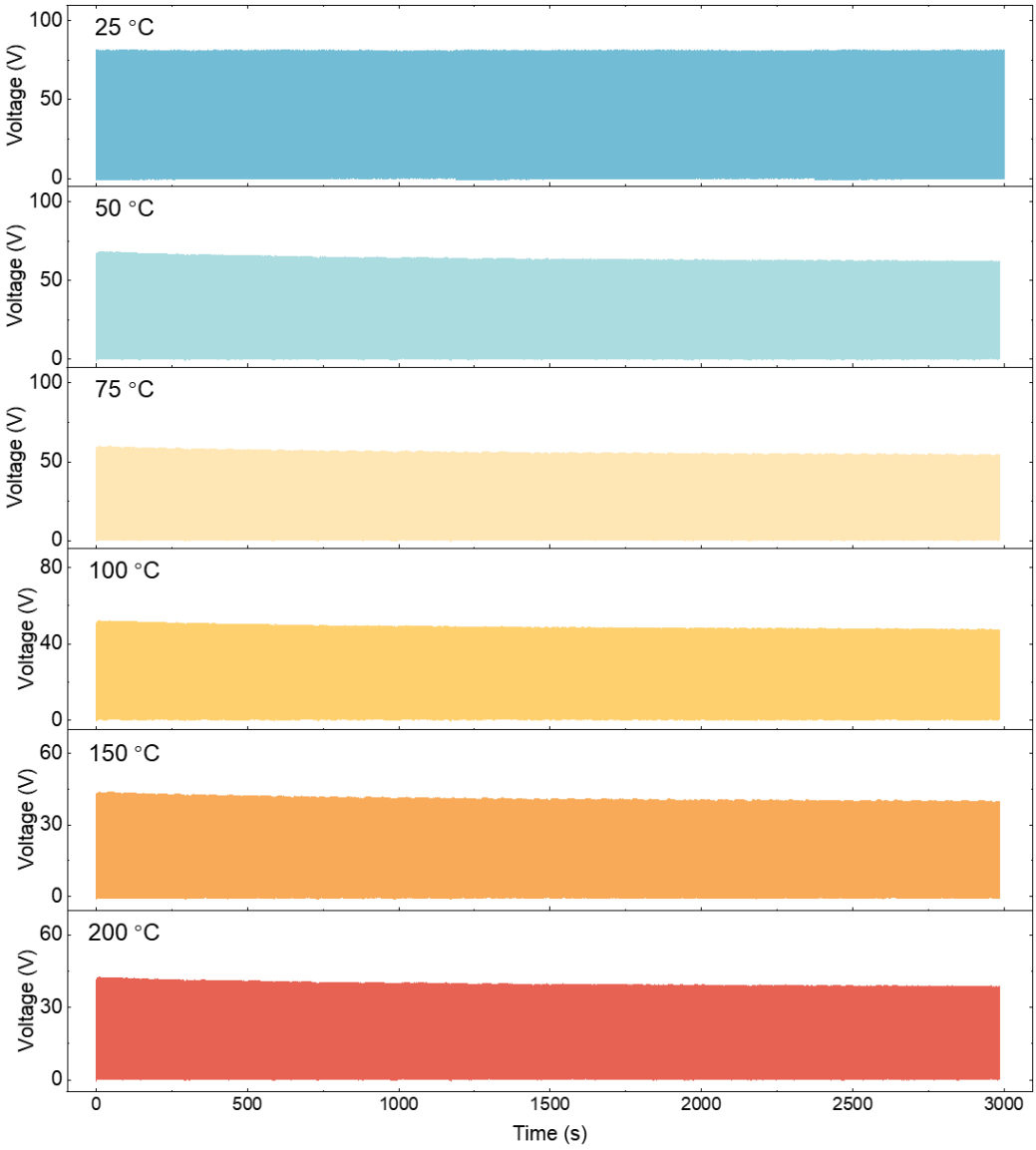

Supplementary Figure 27. The output voltage of TENG based on CNF-III@Si aerogel under cyclic testing at different temperatures, with a frequency of 2.0 Hz.

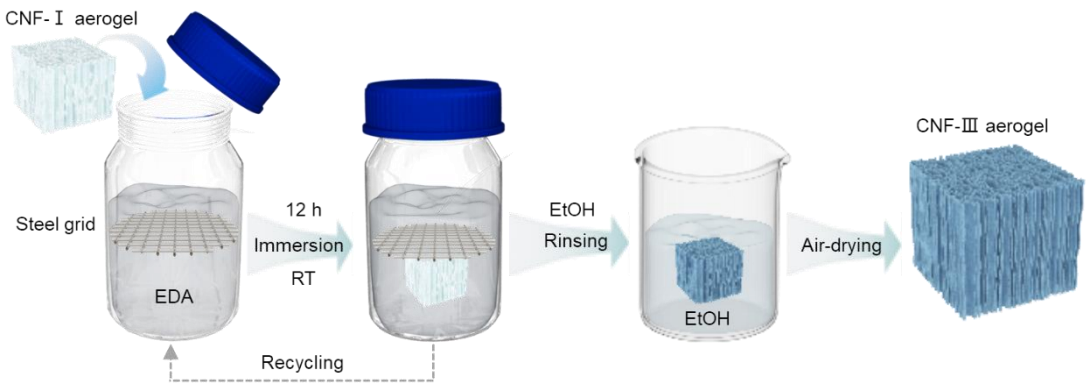

Supplementary Figure 28. The process of preparing CNF-III aerogel by EDA treatment of CNF-I aerogel.

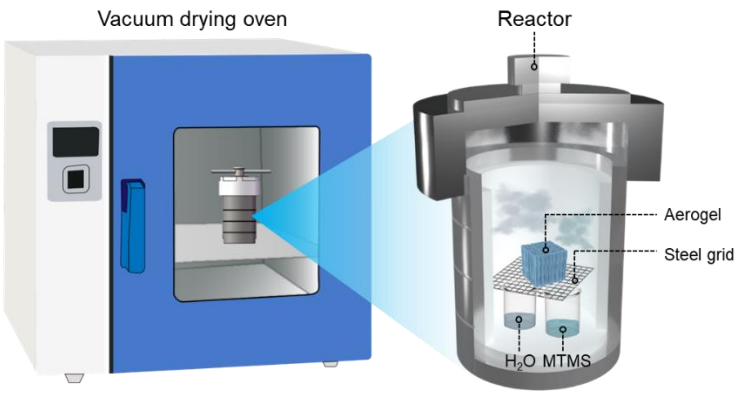

Supplementary Figure 29. Chemical vapor deposition apparatus.

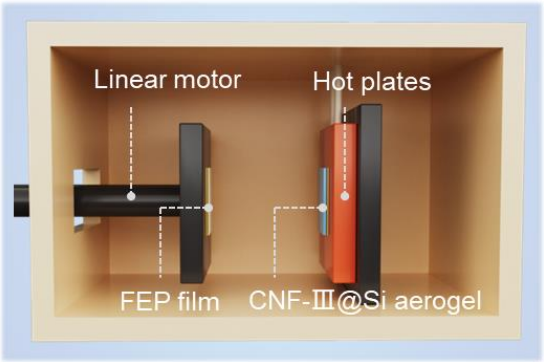

Supplementary Figure 30. High-temperature triboelectric performance testing device.

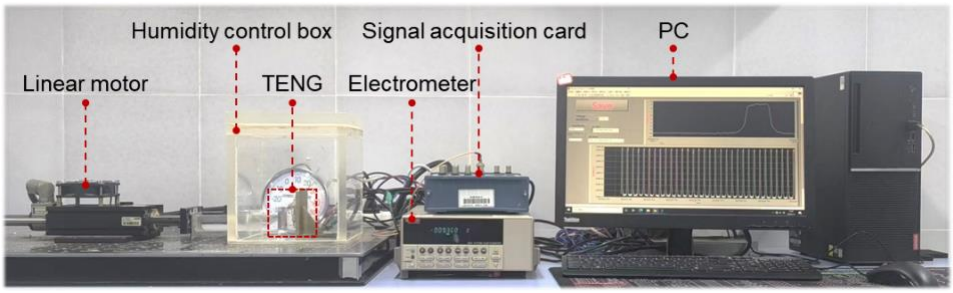

Supplementary Figure 31. Triboelectric testing device under different humidity conditions.

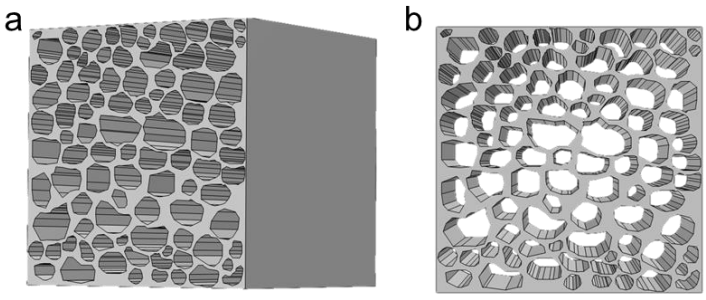

Supplementary Figure 32. 3D honeycomb structure model simulated by finite element method. (**a**) Side view, (**b**) front view.

Supplementary Table 1 to 7

Supplementary Table 1. Summary of mechanical properties and triboelectric performance of triboelectric aerogels reported in the literature.

Materials	Elastic recovery rate (%)	Strength (kPa)	Max. working temperature (°C)	Contact area (cm^2)	V_{oc} (V)	Charge density ($\mu C/m^2$)	Power density ($mW\ m^{-2}$)	Ref.
ZZ-MSCA	38	17.5	-	9	120	48.88	70	13
CNF/PVA	0	2.8 MPa	45		60	67.5	265	14
AS/GO/PVA/CNF	75	155	-	135	34	0.59	-	15
CMPA	78.57%	320	-	4.9	72	97.5	270	16
hierarchical cellulose	95	55	100	529	320	70.89	310	17
TCNF/PVA/CNT	0	69.3	-	7	150	-	220	18
SCMC/CNC	-	130	50	8	132			19
CNF-III@Si	95	180.6	200	4	81.5	32	310	This work

Supplementary Table 2. Molecular dynamics simulation statistics of CNF-I monomer torsion angle

CNF-I	average	standard	RSD (%)	Relative deviation (%)
χ	165.6	170	3.79	-2.59
χ'	-70.61	-70	9.31	0.87
φ	-97.17	-98.5	4.8	-1.35
ψ	-142.28	-142.3	3.53	-0.01

RSD and RD represent the relative standard deviation and relative difference with respect to the literature[4], respectively.

Supplementary Table 3. Molecular dynamics simulation statistics of CNF-III monomer torsion angle

CNF-III	average	standard	RSD (%)	Relative deviation (%)
χ	53.5	44	14.17	21.59
χ'	169.26	163	3.44	3.84
φ	-106.5	-92	7.16	15.76
ψ	-139.38	-146	4.44	-4.53

RSD and RD represent the relative standard deviation and relative difference with respect to the literature[4], respectively.

Supplementary Table 4. Characteristics of different hydrogen bond models obtained from FTIR peak fitting.

Sample	Hydrogen bonds	Wavenumber (cm^{-1})	Content (%)	Bond energy (kJ/mol)	Bond length (pm)
CNF-I	O(2)H…O(6)	3535	7.5	8.28	2.815
	O(3)H…O(5)	3369	66.2	20.15	2.779
	O(6)H…O(3′)	3180	26.3	33.71	2.735
CNF-III	O(2)H…O(6)	3592	10.6	4.16	2.828
	O(3)H…O(5)	3447	64.1	14.56	2.795
	O(6)H…O(3′)	3204	25.3	31.98	2.741

Supplementary Table 5. Test data from an inductively coupled plasma optical emission spectrometer (ICP-OES).

Samples	m_0 (g)	V_0 (mL)	C_0 (mg/L)	f	C_1 (mg/L)	C_x (mg/kg)	W (%)
CNF-I@Si	0.0464	20	1.9153	10	19.1532	8255.69	0.8256%
CNF-III@Si	0.0485	20	3.5062	10	35.0620	14458.56	1.4459%

Calculation of Si content:

$$C_x = \frac{C_0 f V_0}{m_0} = \frac{C_1}{m_0} \tag{9}$$

$$W(\%) = \frac{C_x}{10^6} \times 100\% \tag{10}$$

where m_0 represents the sample mass, V_0 denotes the volume following digestion and final volume adjustment, f indicates the dilution factor, C_1 refers to the ratio of element concentration in the digestion solution to that in the original sample solution, C_x signifies the tested concentration, and W represents the element content in the final sample.

Supplementary Table 6. Crystal unit cell parameters for CNF-I

CNF-I	average	standard	RSD (%)	RD (%)
a	7.585	7.784	3.07	-2.56
b	8.115	8.201	2.17	-1.05
c	11.075	10.38	0.88	6.70
α	92.855	90	6.99	3.17
β	88.915	90	2.1	-1.21
γ	98.075	96.5	2.74	1.63

RSD and RD represent the relative standard deviation and relative difference with respect to the literature[4], respectively.

Supplementary Table 7. Crystal unit cell parameters for CNF-III

CNF-III	average	standard	RSD (%)	RD (%)
a	4.34	4.45	4.4	-2.47
b	7.835	7.85	0.98	-0.19
c	11.097	10.31	9	7.63
α	92.945	90	11.69	3.27
β	88.465	90	3.67	-1.71
γ	113.445	105.1	4.07	7.94

RSD and RD represent the relative standard deviation and relative difference with respect to the literature[4], respectively.

Supplementary References

1. Pan, J., Hamad, W. & Straus, S. K. Parameters affecting the chiral nematic phase of nanocrystalline cellulose films. *Macromolecules* **43**, 3851–3858 (2010).

2. Nishiyama, Y., Sugiyama, J., Chanzy, H. & Langan, P. Crystal Structure and Hydrogen Bonding System in Cellulose Iα from Synchrotron X-ray and Neutron Fiber Diffraction. *J. Am. Chem. Soc.* **125**, 14300–14306 (2003).

3. Wada, M., Chanzy, H., Nishiyama, Y. & Langan, P. Cellulose III_I crystal structure and hydrogen bonding by synchrotron X-ray and neutron fiber diffraction. *Macromolecules* **37**, 8548–8555 (2004).

4. Wada, M., Nishiyama, Y. & Langan, P. X-ray structure of ammonia-cellulose I: New insights into the conversion of cellulose I to cellulose III_I. *Macromolecules* **39**, 2947–2952 (2006).

5. Zhang, M., Geng, Z. & Yu, Y. Density Functional Theory (DFT) Study on the Dehydration of Cellulose. *Energy & Fuels* **25**, 2664–2670 (2011).

6. Wang, Q. *et al.* Initial pyrolysis mechanism and product formation of cellulose: An Experimental and Density functional theory (DFT) study. *Sci. Rep.* 10, 3626 (2020).

7. Lu, X. *et al.* Cellulose dissolution in ionic liquid from hydrogen bonding perspective: first-principles calculations. *Cellulose* **30**, 4181–4195 (2023).

8. Delley, B. From molecules to solids with the DMol3 approach. *J. Chem. Phys.* **113**, 7756–7764 (2000).

9. Perdew, J. P., Burke, K. & Ernzerhof, M. Generalized Gradient Approximation Made Simple. *Phys. Rev. Lett.* **77**, 3865–3868 (1996).

10. Zhang, J. *et al.* Advanced enzyme-assembled hydrogels for the remediation of contaminated water. *Nat. Commun.* **16**, 3050 (2025).

11. Wan, J., Lian, J., Wang, Y. & Ma, Y. Investigation of cellulose supramolecular structure changes duringconversion of waste paper in near-critical water on producing5-hydroxymethyl furfural. *Renew. Energy* **80**, 132–139 (2015).

12. Yeh, F., Hsiao, B. S., Sauer, B. B., Michel, S. & Siesler, H. W. In-Situ Studies of Structure Development during Deformation of a Segmented Poly(urethane−urea) Elastomer. *Macromolecules* **36**, 1940–1954 (2003).

13. Su, J. *et al.* Superelastic Triboelectric Aerogel Enabled by Cross-Scale Fibers and Heterojunction Particles for Wearable Intelligent Neck Guard. *Adv. Funct. Mater.* **33**, e15065 (2025).

14. Luo, B. *et al.* Multiscale Structural Nanocellulosic Triboelectric Aerogels Induced by Hofmeister Effect. *Adv. Funct. Mater.* **33**, 2306810 (2023).

15. Wu, X. *et al.* Elastic Yet Strength Triboelectric Aerogel Enabled by Constructing a Supramolecular System. *Adv. Funct. Mater.* **35**, 2417067, (2024).

16. Meng, N. *et al.* Monolithic Conjugated Microporous Polymer Aerogel for Triboelectric Nanogenerator. *Adv. Funct. Mater.* **34**, 2313534 (2024).

17. Zhong, S. *et al.* Passive Isothermal Flexible Sensor Enabled by Smart Thermal-Regulating Aerogels. *Adv. Mater.* **37**, 2415386 (2025).

18. Gao, C. *et al.* Hierarchical porous triboelectric aerogels enabled by heterointerface engineering. *Nano Energy* **121**, 109223 (2024).

19. Cai, C. *et al.* Lightweight and Mechanically Robust Cellulosic Triboelectric Materials for Wearable Self-Powered Rehabilitation Training. *ACS Nano* **19**, 396–405 (2025).